Materials Horizons

Accepted Manuscript

This article can be cited before page numbers have been issued, to do this please use: Y. Meng, Z. Pu, Y. Qi, Y. Zhang, S. Xing, X. Yi, S. Wang, S. Liu and N. Wu, *Mater. Horiz.*, 2026, DOI: 10.1039/D6MH00559D.

ROYAL SOCIETY OF CHEMISTRY

rsc.li/materials-horizons

View Article Online
DOI: 10.1039/D6MH00559D

New concepts

The prevailing paradigm for constructing superhydrophobic anti-icing surfaces relies on precisely engineering the coating formulation with high nanoparticle loadings, intricate chemical modifications, and complex multi-step processing. This work challenges that paradigm by introducing a substrate-driven design strategy, where the structural outcome is governed not by the spray slurry, but by the received substrate. Using a porous fibrous film as an active assembly medium, nanoparticles are selectively retained and spontaneously organized into a fine nanoporous architecture in a single spraying step. This transforms the substrate from a passive mechanical support into a programmable morphological regulator, enabling robust superhydrophobicity at only 2.5 wt% nanoparticle content. The design principle is generalizable beyond specific materials, as demonstrated by successful structure formation with varied solvents and resins. Furthermore, this strategy seamlessly integrates with the standard manufacturing processes of resin-based composites, unlocking a scalable and cost-effective pathway to high-performance anti-icing solutions for aircraft, wind turbine blades, and cryogenic fuel storage.

View Article Online
DOI: 10.1039/D6MH00559D

All data generated or analyzed during this study are included in this published article and its supplementary information (SI).

View Article Online
DOI: 10.1039/D6MH00559D

Scalable nanoporous superhydrophobic films toward extreme icing conditions at −141°C and icing wind tunnel

Yunyun Meng, [a] Zhengang Pu, [a] Yang Qi, [a] Yanxin Zhang, [b] Suli Xing, [*a] Xian Yi, [*b] Song Wang, [a] Senyun Liu [b] and Nan Wu[*a]

a: College of Aerospace Science and Engineering, National University of Defense Technology, Changsha, Hunan, 410073, China
E-mail: happy_xing@nudt.edu.cn; lierenwn@nudt.edu.cn
b: Key Laboratory of Icing and Anti/De-Icing, China Aerodynamics Research and Development Center, Mianyang, Sichuan, 621000, China
E-mail: yixian_2000@163.com

Abstract

Superhydrophobic surfaces offer a promising passive anti-icing alternative, yet they frequently fail to sustain the non-wetting Cassie-Baxter state under dynamic icing conditions. Conventional approaches for robust superhydrophobic anti-icing coating rely on high nanoparticle loadings (>50 wt%) to achieve the desired nanoporous roughness, often compromising cost efficiency and interfacial robustness. Herein, we proposed a novel and practical substrate-driven spraying strategy to construct fine nanoporous structures, allowing superhydrophobicity at a substantially reduced nanoparticle content of 2.5wt%. The optimized nanoporous superhydrophobic films exhibited excellent dynamic anti-icing performance, effectively repelling impacting droplets at −141°C and suppressing long-term condensation for over 3 h. Furthermore, the dynamic deicing behaviors are confirmed by the high slipperiness of melted ice and coalescence-induced wriggling of melting ice/frost. When integrated into composite airfoils, the film surface exhibits outstanding practical

View Article Online
DOI: 10.1039/D6MH00559D

efficacy in icing wind tunnel tests. Only 0.4 W/cm^2 of power density was required to suppress icing at both the leading edge and runback zone. This work offers a promising pathway for implementing high-performance anti-icing solutions in advanced resin-based composite materials in wind turbine blades, aircraft, and cryogenic fuel storage tanks.

Keywords

anti-wetting, dynamic, anti-icing/deicing, nanostructures, superhydrophobic films, spraying

1. Introduction

Ice accretion poses a severe and persistent threat to resin-based composite materials operating in low-temperature environments, such as wind turbine blades, advanced aircraft, and cryogenic fuel storage tanks, often leading to performance degradation and catastrophic failures.[1] Traditional anti-icing and de-icing technologies based on mechanical or thermal effects are energy-intensive and rely on complex ancillary systems.[2] In response, the development of passive, energy-free alternatives has become a focal point of research.[3, 4] Among these, superhydrophobic surfaces that leverage the non-wetting Cassie-Baxter (C-B) state to retard water/ice formation have shown considerable promise for static anti-icing.[5] However, under dynamic icing environments featuring high undercooling, elevated humidity, and ultra-low temperatures, previously reported superhydrophobic surfaces frequently fail to sustain the stable C-B state.[6] Consequently, they usually fail to pass rigorous icing wind tunnel assessments.[7] Under these extreme icing conditions, the surface is exposed to both impacting and condensed water droplets. These droplets tend to penetrate and pin within the micro/nanostructures, promoting the formation of tenacious,

View Article Online
DOI: 10.1039/D6MH00559D

interlocked ice.[8, 9] Consequently, enhancing the robustness of the superhydrophobic state under extreme dynamic icing conditions remains a paramount challenge.[10]

The wetting state under icing conditions is governed critically by the vapor-liquid phase transition and the subsequent dynamics of condensate water.[11] Various engineered surfaces have been developed to manipulate these dynamic processes for applications such as atmospheric water harvesting and dropwise condensation.[12, 13] In most cases, these reports together highlight the importance of nanostructures in facilitating the highly slippery C-B state.[14] Indeed, nanostructures consistently exert their effect in inhibiting the formation and accumulation of both water and ice.[15, 16] Specifically, during condensation, they have been demonstrated to inhibit the nucleation of condensate droplets,[17] enhance droplet mobility,[18] and facilitate rapid shedding.[19] While under water impact conditions, nanostructures contribute to minimizing contact angle hysteresis and energy dissipation,[20] thereby increasing the possibility of droplet rebound. Therefore, the superhydrophobic surface incorporating with fine nanostructures exhibits a dual-repellency capability, effectively shedding water at both the micro-scale condensate water and the macro-scale impacting droplets.

However, the scalable and portable preparation of the requisite fine nanostructures presents another significant hurdle. Existing top-down techniques like corrosion[21] and photolithography,[22] as well as bottom-up methods such as sol-gel,[23] self-assembly,[24] and physical vapor deposition,[25] can create nanostructures on the flat or micro-structured surfaces. However, these techniques are often hampered by complexity, high cost, and time-consuming.[26, 27] Notably, candle soot, multi-wall/single-wall carbon nanotubes, and fumed silica are common nanomaterials for fabricating fine nanostructures.[28, 29] Air-

View Article Online
DOI: 10.1039/D6MH00559D

assisted spraying enables the deposition of structured superhydrophobic coatings onto diverse substrates using these nanoparticles.[30, 31] Given this versatility, along with its inherent scalability, the technique is a promising candidate for the large-scale surface engineering of composite materials. Nevertheless, adding binders to enhance adhesion strength may reduce the exposure of nanostructures at the coating surface.[32] Advanced technologies have been developed to regulate the deposition morphology, such as electrostatic spraying,[33] ultrasonic spraying,[34] flame spraying,[35] and thermal spraying.[36] However, achieving binder-minimized superhydrophobic surfaces in a facile and scalable manner remains elusive.

In this work, we examine the critical requirements for superhydrophobic surfaces to achieve dynamic anti-wetting and anti-icing, pinpointing fine nanopores and nano-architectures as essential features. We subsequently propose a facile substrate-driven morphology control strategy to construct such desirable nanoporous films, which enables superhydrophobicity at a substantially reduced nanoparticle content of 2.5 wt%. This method breaks through the dependence of the traditional superhydrophobic structure spraying process on high nanoparticle content. The optimized nanoporous superhydrophobic structures exhibit exceptional dynamic anti-icing performance, capable of repelling water droplets impacting on surfaces cooled below −140°C and withstanding prolonged vapor condensation for 3 h. Moreover, we elucidated the superior of nanoporous structures to maintain superhydrophobic stability in the dynamic deicing process under the coupling of gravity and thermal effects. Importantly, the resulting nanoporous superhydrophobic film can be integrated into the resin-based composite airfoil without altering its standard manufacturing process.[37] Subsequent icing wind tunnel tests confirmed

View Article Online
DOI: 10.1039/D6MH00559D

the practical anti-icing capability with low energy consumption at 0.4 W/cm^2. Our findings tackle both the scientific and practical bottlenecks in implementing advanced anti-icing technology for resin-based composites, particularly in the demanding fields of aerospace and wind energy.

2. Results and Discussion

2.1. Anti-Icing Performances of Nanoporous Structures

Nanoporous structures with fine nanopores and nano architectures hold groundbreaking potential for anti-icing applications through the following anti-wetting mechanisms (Fig. 1a). First, nanoporous structures can inhibit the phase transition of water vapor to condensate droplets by regulating the vapor pressure. For a hydrophobic nanocavity ($\cos\theta<0$), Kelvin equation dictates that the vapor pressure inside the cavity (P_r) is higher than the ambient saturation vapor pressure (P_{sat}) (Fig. 1b). When the cavity size is smaller than 100 nm, the elevated vapor pressure will help stabilize the vapor phase and suppress condensation (Supplementary Note S1).[38, 39] Second, when water vapor condenses to form liquid water, the fine nanoporous structure also shows strong superhydrophobicity to facilitate water shedding. As shown in Fig. 1c, when a droplet resides on the nanoporous surface in the C-B state, the apparent contact angle increases with decreasing solid-liquid contact fraction. The nanoporous structures enable outstanding superhydrophobicity due to the minimal solid-liquid contact area (Supplementary Note S1). Third, the triple-phase contact lines (TPCL) on such nanoporous structures are short and discontinuous (Fig. 1a). This contributes to very low contact angle hysteresis (CAH),[40, 41] which is critical for maintaining the non-wetting state under dynamic water exposure. Fourth, nanoporous structures exhibit high thermal resistance to suppress solid-liquid heat transfer, thereby

View Article Online
DOI: 10.1039/D6MH00559D

reducing excessive energy dissipation in droplets (Fig. 1a). In contrast to the sparse air pockets trapped by conventional roughness, the high porosity of nanoporous structures entraps a much larger air volume. This endows them with superior overall thermal insulation performance. In fact, owing to the mechanisms discussed above, nanoporous structures are effective in suppressing the generation, accumulation, and infiltration of liquid water from the microscopic to the macroscopic scale (Fig. S1). This cross-scale anti-wetting capability forms the basis for effective dynamic anti-icing.[42]

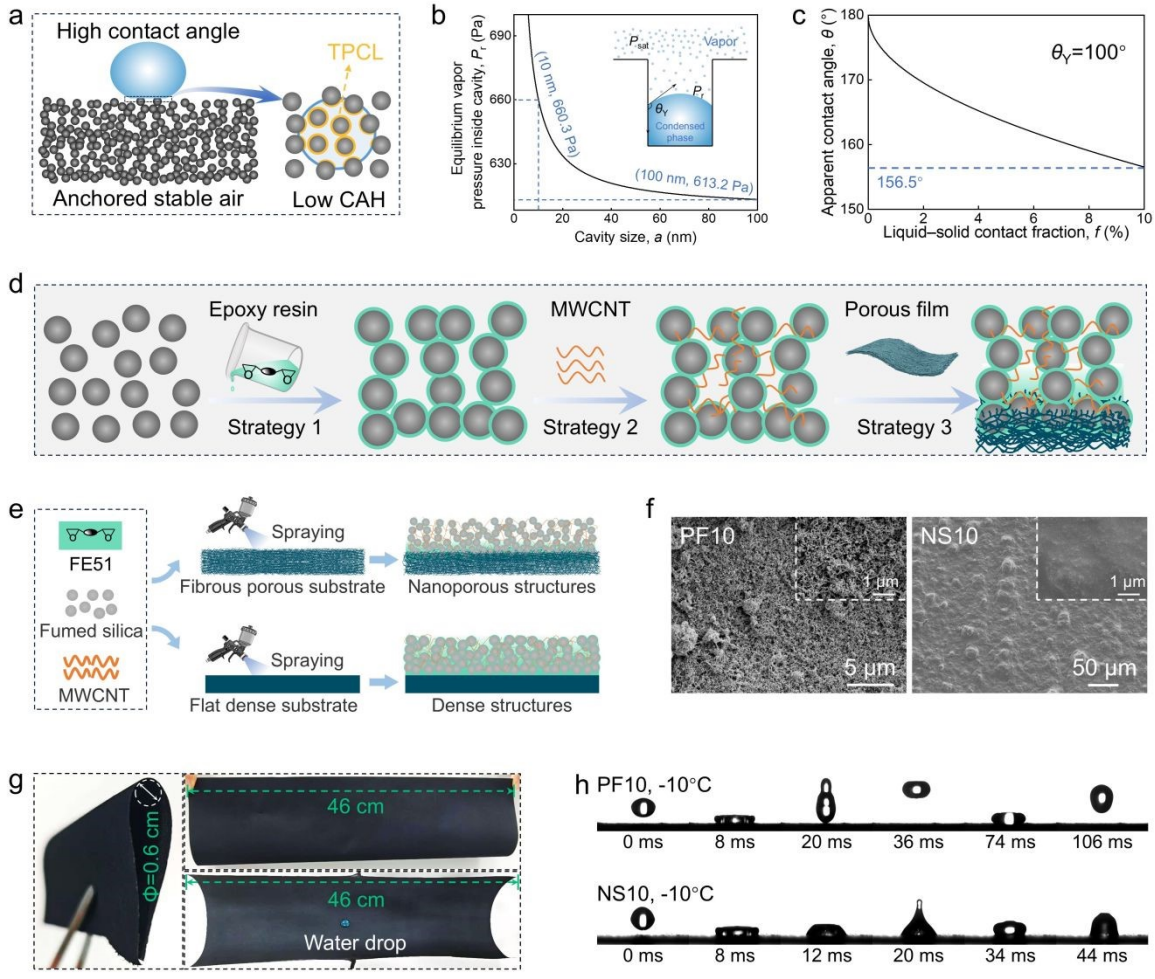

Fig. 1 (a) Schematic diagram of the anti-icing mechanisms of nanoporous structures. (b) The variation of vapor pressure inside the cavity (P_r) with cavity size (a). (c) Change of the apparent contact angle with the liquid-solid contact fraction for the ideal Cassie-Baxter

View Article Online
DOI: 10.1039/D6MH00559D

state. (d) Three complementary strategies for constructing robust nanoporous structures. (e) Schematic diagram of the distinct spray deposition morphology on nonporous substrate (NS) and porous fibrous film (PF) substrates. (f) SEM images of prepared NS10 and PF10. (g) Optical photos demonstrating the flexibility and retained superhydrophobicity of a bent PF10 film. (h) Snapshots of droplets impacting the surfaces of PF10 and NS10 at −10°C.

However, the scalable and low-cost fabrication of such fine nanoporous structures remains a significant challenge.[27] Commercially available fumed silica nanoparticles, with primary particle sizes of 4-40 nm, serve as an ideal building block for this purpose. Herein, we integrate three complementary strategies to prepare robust nanoporous structures based on these nanoparticles (Fig. 1d). Firstly, fluorinated epoxy resin is added as a binder to construct a cohesive nanoparticle skeleton, the so-called "resin + particle" strategy.[43] The resin content is critical as a trade-off must be struck between skeleton strength and porosity. Generally, the nanoparticles are likely to be wrapped and covered with resin, causing nonporous dense structures.[44] Although higher nanoparticle content can improve surface roughness, it may lead to insufficient adhesion between nanoparticles and between coatings and substrates.[45] To address this, our second strategy incorporates high-aspect-ratio multi-walled carbon nanotubes (MWCNTs) to reinforce the connectivity and strength within the nano-architecture. Last but not least, we employ the porous fibrous film (PF) as a spraying substrate (Fig. S2a), which represents a departure from conventional formulation-centric approaches.[46] In this design, the porous fibrous substrate is hypothesized to facilitate the formation of nanoporous structures while simultaneously establishing a robust anchored interface, as shown in Fig. 1e. To implement the above three strategies, the fumed silica, MWCNTs, and fluorinated E51 epoxy resin (FE51) were mixed to obtain a slurry, and followed by assembling it into nanoporous structures through spray process (Fig. 1e).

View Article Online
DOI: 10.1039/D6MH00559D

It is important to note that the nanoporous structures are fundamentally distinct from previously reported superhydrophobic coatings on other substrates. Although heterogeneous substrates have been employed in previous studies, they are largely selected either to achieve mechanical flexibility or to improve interfacial adhesion. Consequently, conventional combinations of spray slurries and substrates do not yield the targeted fine nanoporous architecture (Fig. S3). However, this substrate employed in our strategy features a nanoscale porous fibrous structure, which represents not merely a processing method, but a design rationale and a viable strategy for constructing nanostructured coatings.

As shown in Fig. 1f, aerosolized slurry with nanoparticle content of only 10 wt% tends to form fine nanoporous structures on the PF film. Dynamic water repellency was characterized by impacting ~10 μL water droplets from a 10 cm height. The inherent hydrophilicity of the bare PF substrate led to droplet adhesion (Fig. S4a). In contrast, after depositing a nanoporous coating via spraying, the resulting PF10 surface enables complete rebound of impacting droplet (Fig. S4b). Furthermore, through co-curing and hot-pressing with prepreg, the PF10 can be integrated into a composite airfoil (denoted as PF10-airfoil) with the preservation of excellent dynamic water repellency (Fig. S4c). Additionally, the PF10 sample retains its superhydrophobicity even under severe bending deformation (Fig. 1g), highlighting its mechanical robustness and potential for use in conformal or curved aerodynamic components. The critical role of the substrate becomes unequivocally clear when the same slurry is sprayed onto a composite laminate surface (Fig. S2b) as a nonporous substrate (NS). In this case, it yields a dense, nonporous structure (Fig. 1f). At room temperature, the NS10 surface appears superhydrophobic, while this non-wettability

View Article Online
DOI: 10.1039/D6MH00559D

severely degrades under low-temperature dynamic conditions. To demonstrate this, both PF10 and NS10 were cooled to −10°C and impacted by droplets from a height of 10 cm. As shown in Fig. 1h, the droplet completely rebounded from the PF10 surface, whereas it was pinned on the NS10 surface. A top-down perspective coupled with infrared thermography further confirmed this anti-wetting difference (Fig. S5, Movies S1 and S2). Notably, the impacting droplet effectively cleared the condensed water from the PF10 surface, providing direct evidence of a stable low-adhesion C-B state.[47] This substrate-dependent divergence in anti-wetting and anti-icing performance is often overlooked but profound. Given the prevalent challenge of superhydrophobic degradation at low temperatures, our substrate-driven spraying strategy represents a groundbreaking, simple, and readily executable advance.

2.2. Substrate-Driven Regulation of Morphology and Wettability

Regulating surface morphology through substrate selection presents a facile and highly effective alternative to conventional spraying strategies. This approach circumvents the typical reliance on high nanoparticle loadings to achieve micro/nano-roughness. Remarkably, even at a nanoparticle content as low as 2.5 wt%, PF2.5 exhibits well-defined nanostructures (Fig. 2a), whereas NS2.5 shows a comparatively smooth and dense morphology with insufficient roughness (Fig. 2b). These distinct morphologies, arising directly from the different deposition dynamics of the aerosolized slurry on porous versus nonporous substrates, lead to profound differences in wettability. Achieving spray-coated superhydrophobicity on conventional substrates typically requires a high nanoparticle loading (>30%), along with intricate nano-architectural modifications (Supplementary Note S2, Table S1). Our strategy overcomes this by utilizing a significantly lower

View Article Online
DOI: 10.1039/D6MH00559D

nanoparticle content. This reduction translates directly into cost efficiency and enhanced interfacial adhesion strength.

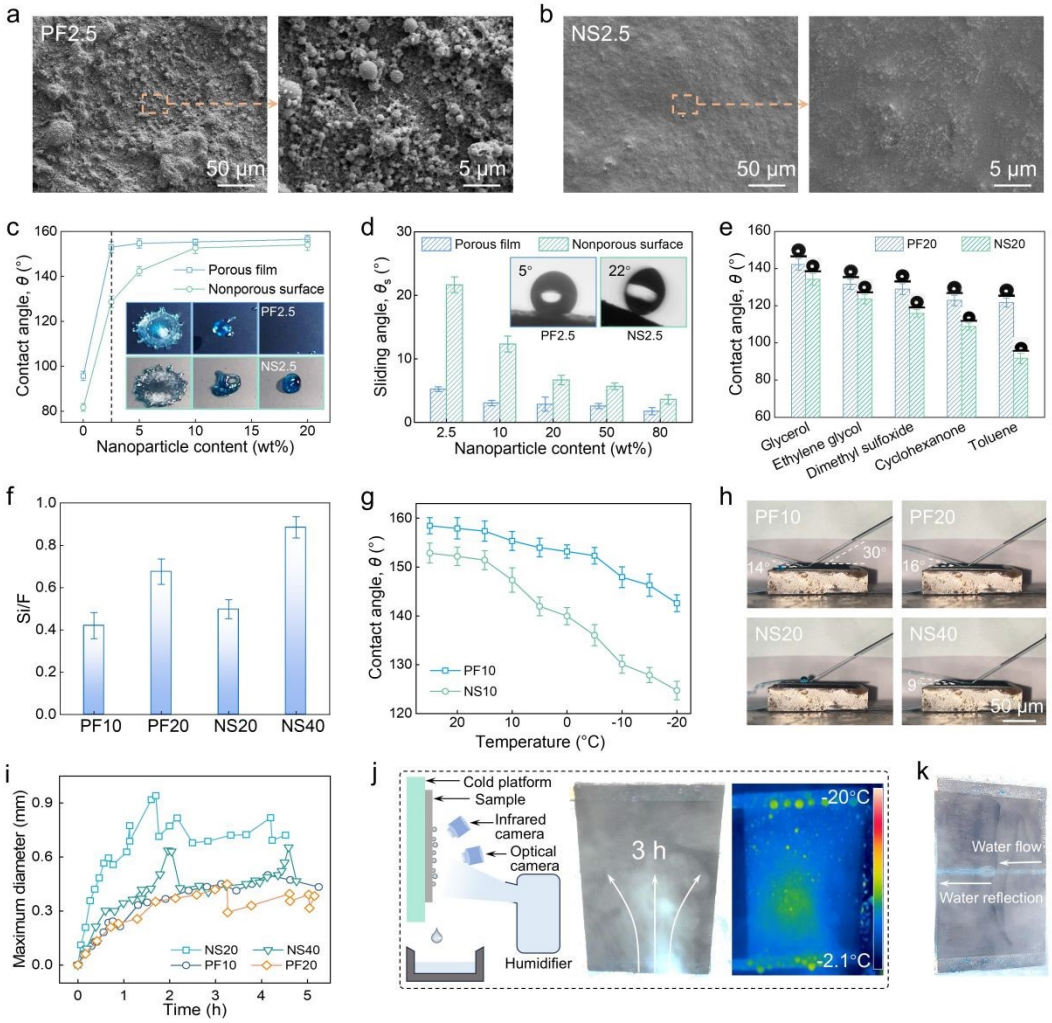

Fig. 2 SEM images of prepared surfaces with only 2.5 wt% nanoparticles on (a) porous film (PF2.5) and (b) nonporous substrate (NS2.5). (c) Water CAs and (d) water SAs as a function of nanoparticle content for PF and NS substrates. (e) CAs of various organic solvents on PF20 and NS20 surfaces. (f) Surface Si/F atomic ratio from EDS analysis, indicating nanoparticle exposure. (g) Water CAs of PF10 and NS10 changing with surface temperature. (h) Dynamic water jet repellency test from an incident angle of 30° at −20°C. (i) Variation of the maximum diameter of condensate droplets with time on different sample surfaces. (j) Schematic diagram, optical image, and the corresponding infrared

View Article Online
DOI: 10.1039/D6MH00559D

photo of the anti-condensation test in high humidity environment. (k) Optical image of PF10 surface exhibiting waterjet impacting after 3-h anti-condensation test.

The influence of the substrate on wettability is quantitatively demonstrated by the water contact angles (CAs) and sliding angles (SAs) of prepared films with varying nanoparticle content (Fig. 2c-d). Sprayed structures on the PF substrate consistently achieve higher CAs and lower SAs than their NS counterparts at equivalent loadings. When the nanoparticle content was reduced to 2.5 wt%, PF2.5 exhibited superhydrophobicity with water CA of 153±2.5° and water SA of 5.2±0.4°, hence repelling impacting droplet from the height of ~10 cm (Fig. 2c). As a sharp contrast, the NS2.5 failed to reach the threshold of superhydrophobicity with water CA of 128.7±2.6° and water SA of 21.7±1.2°, resulting in the final pinning of the impact droplet. Even though differences in water CA and water SA diminish at nanoparticle contents above 10 wt%, the intrinsic wettability contrast persists, as revealed by contact angles of various organic solvents (Fig. 2e). For every solvent tested, PF20 displays a higher contact angle than NS20. Notably, this disparity becomes more pronounced for liquids with lower surface tension. For the toluene with surface tension of 28.9 mN/m, the CAs are 121.7±2.4° for PF20 versus 91.7±2.8° for NS20, underscoring the more effective liquid repellency imparted by the PF-derived nanostructures.

To elucidate the mechanism behind this substrate-driven morphology control, we analyzed both the surface topography and the compositional distribution of the coatings. First of all, SEM analysis confirmed that the thermal curing process did not alter the spraying morphology (Fig. S6), indicating that the differentiated topography is dictated solely by the slurry deposition process. Furthermore, when the ethyl acetate solvent was replaced by N, N-dimethylformamide (DMF), or the fluorinated epoxy resin (F-E51) was

View Article Online
DOI: 10.1039/D6MH00559D

replaced with polydimethylsiloxane (PDMS), similar nanoporous structures were successfully obtained (Fig. S7). Therefore, the proposed substrate-driven strategy does not depend on a specific slurry formulation, but rather on its regulation of the self-assembly process of the slurry during deposition. Since the actual deposition process cannot be directly observed, we employed EDS to analyze the surface elemental distribution of PF10, PF20, NS20, and NS40 (Fig. S8). We focused on the Si (from SiO_2 nanoparticles) and F (from the fluorinated epoxy resin) signals (Fig. S9). The Si/F ratio serves as a quantitative indicator of the relative surface exposure of nanoparticles. As shown in Fig. 2f, the Si/F ratio increases with nanoparticle content for both NS and PF substrates, which aligns with the expected results. Crucially, for any given content, the Si/F ratio is consistently higher for coatings on the PF substrate than on the NS substrate. This provides direct evidence that the PF substrate promotes greater nanoparticle exposure. This is corroborated by observing early-stage deposition (Fig. S10). A minimal amount of slurry forms a dispersed, nanoparticle-rich porous network on the PF substrate, but a resin-encapsulated, smoother film on the NS substrate. This fundamental difference in initial growth dictates the final morphology, which is preserved with further spraying. These observations support a proposed mechanism in which the PF substrate acts as a filter during spraying. It rapidly absorbs the solvent and partially the resin from the spraying slurry, concentrating and retaining the nanoparticles at the deposition front. This process facilitates the in-situ assembly of a nanoporous structure. Therefore, it should be emphasized that the reported nanoparticle loading refers to the slurry composition as a controlled input parameter rather than a descriptor of the final surface composition.

View Article Online
DOI: 10.1039/D6MH00559D

It should be emphasized that the mechanism described above represents a generalized interpretation based on our current observations. The underlying assembly process may also involve Brownian motion of resin molecules and heterogeneous aggregation during the drying of the liquid film. Notably, when other porous substrates were employed, including foam iron, filter paper, wire mesh, and fabric, none were able to produce the desired fine nanoporous structure (Fig. S3). This indicates that simply using a porous substrate to enhance the absorption of resin and solvent does not universally lead to the target coating morphology. The outcome appears to be closely related to the characteristic dimensions of the substrate, because a substrate of carbon nanotube film prepared by vacuum filtration yields a similar nanoporous structure. Collectively, scalable fabrication of such fine nanoporous anti-icing surfaces is far from a straightforward engineering implementation. The underlying mechanisms are highly complex and warrant further investigation.

The superhydrophobic superiority of the fine nanostructures on PF substrates is further magnified under low-temperature conditions, which are critical for dynamic anti-icing performance. As expected, both PF10 and NS10 exhibit a reduction in contact angle with decreasing surface temperature (Fig. 2g). This common phenomenon is attributed to condensation within the structures in a supersaturated vapor environment.[38] However, PF10 demonstrates far greater resilience, whose CA remains higher than that of NS10 at every temperature, and the decline rate is significantly slower. For instance, the PF10 maintained superhydrophobicity at −5°C with a water CA of 152.3±1.7°, while the NS10 fell below this threshold even at 10°C with a water CA of 147±2.5°. This indicates that the

View Article Online
DOI: 10.1039/D6MH00559D

nanoporous structure of PF10 is more effective at resisting water penetration and condensation-induced wetting transitions.

Static contact angles alone are insufficient to evaluate anti-icing performance under dynamic icing conditions. Therefore, we assessed the uniformity and effectiveness of dynamic water repellency using a water jet test at −20°C (Fig. 2h). When a water jet impinged on the surfaces at an incidence angle of ~30°, it was cleanly reflected from the PF10, PF20, and NS40 surfaces at angles of approximately 14°, 16°, and 9°, respectively. In stark contrast, the water jet adhered to and accumulated on the NS20 surface. These results unambiguously demonstrate that spraying structures on the PF substrate possess superior dynamic anti-wetting properties under low-temperature icing conditions compared to those on the NS substrate.

Vapor condensation in the high-humidity, low-temperature icing environment often leads to superhydrophobic degradation and a loss of dynamic anti-wetting capabilities. We evaluated long-term anti-condensation performance by monitoring droplet growth on surfaces held at −5±1°C for 5 h (Fig. S11a). Tracking the maximum droplet diameter over time reveals distinct shedding behaviors (Fig. 2i), whose abrupt changes represent detachment or coalescence events. For NS20 and NS40, droplets grew to relatively large sizes (~0.94 mm and ~0.64 mm, respectively) before abrupt detachment (Fig. S11b), exhibiting the characteristic of gravity-driven sliding (Fig. S12a). In contrast, on PF10 and PF20 surfaces, the maximum droplet diameter stabilized at a much smaller value (~0.45 mm) after about 3.2 h. Clearly, the fine nanoporous structures enables condensate droplets maintaining a low-adhesion C-B state.[48] Consequently, they depart via coalescence-induced jumping at a much smaller size and earlier stage (Fig. S12b), a more efficient

View Article Online
DOI: 10.1039/D6MH00559D

shedding mechanism than gravity-driven sliding. Furthermore, we conducted a macroscopic validation of the superhydrophobic durability against condensation. As shown in Fig. 2j, the surface of PF10 cooled at −5°C was exposed to a flux of humid air for 3 h to promote surface condensation, and the waterjet impact was subsequently utilized to test the surface wettability. As shown in Fig. 2k and Movie S3, the water jet was cleanly repelled without any adhesion, demonstrating that the nanoporous structure of PF10 retains excellent dynamic non-wetting properties even after prolonged exposure to a condensing environment.

2.3. Dynamic Anti-Icing at Extreme Conditions

Maintaining a non-wetting state at ultralow temperatures poses severe challenges for superhydrophobic surfaces, primarily due to drastically increased water viscosity and intensified vapor condensation, both of which compromise the stability of the C-B state. To probe the dynamic anti-icing limits, we employed liquid nitrogen to cool sample surfaces to below −100°C (Fig. 3a). Surface temperature was monitored in real-time using a PT100 thermometer (Fig. S13a, Movie S4). The temperature of the solid-liquid impact zone can't be monitored in real time because such ultralow temperatures lie beyond the operational range of existing infrared cameras. To verify the reliability of the reported temperature, four PT100 sensors were attached at different locations on the sample surface, including the central point where the droplet impact occurred. As shown in Fig. S13b, the temperature of the central location was slightly colder than the peripheral areas, with deviations within 5°C, which most likely arises from faster heat conduction at the edges. These results confirm that the temperature measurement error falls within an acceptable range and that the reported surface temperature is essentially reliable. It is noteworthy that

View Article Online
DOI: 10.1039/D6MH00559D

the water impact tests were conducted at a relatively high relative humidity (~55%), significantly exceeding the levels reported in many benchmark studies (Table S2). In this condition, vapor condensation and desublimation are usually inevitable and detrimental to droplet rebound. Strikingly, even when the surface was cooled to an ultra-low temperature of −141°C, a water droplet dropping from a 10 cm height exhibited complete rebound from the PF20 surface (Fig. 3b, Movie S5). In stark contrast, an identical droplet was irreversibly pinned on the NS40 surface at a comparatively higher temperature of −125°C (Fig. 3c, Movie S6). The temperature profiles recorded during these impacts confirm the extreme conditions (Fig. 3d). To contextualize this achievement, we benchmark our results against the state of the art (Fig. 3e, Table S2). Previous reports on superhydrophobic surfaces with single or hierarchical textures demonstrate droplet rebound only at temperatures above approximately −30°C. Our nanoporous surfaces (PF10 and PF20) dramatically extend this limit. To our knowledge, this work is the first to achieve complete rebound of impacting water droplets from surfaces cooled below −100°C.

View Article Online
DOI: 10.1039/D6MH00559D

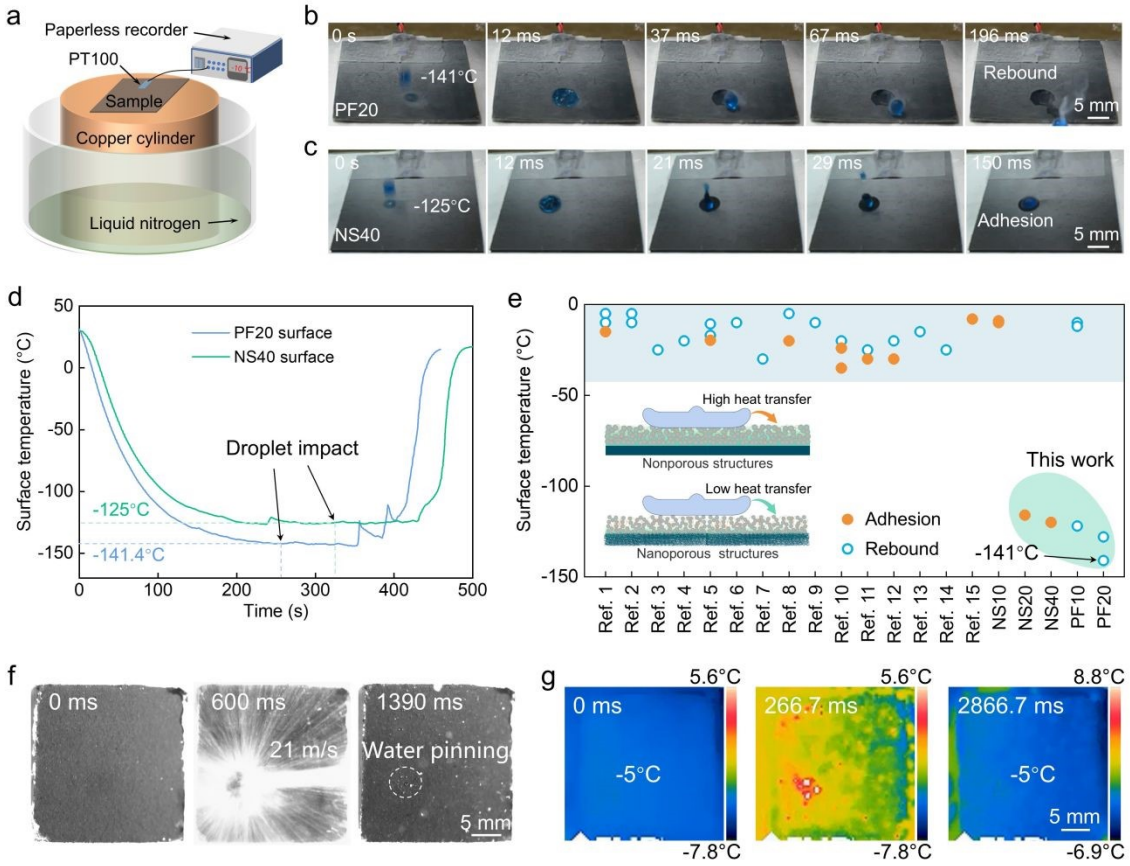

Fig. 3 (a) Schematic diagram of the ultra-low temperature droplet impact test setup using liquid nitrogen cooling. Snapshots of water impact on surfaces of (b) PF20 at −141°C and (c) NS40 −125°C, showing the final rebounding and pinning state, respectively. (d) Temperature curves of the PF20 and NS40 surfaces during water impact tests. (e) Comparison of the tested anti-wetting temperature between our work and the current state-of-the-art superhydrophobic surfaces. Hollow dots denote instances of droplet rebound, whereas solid dots signify droplet adhesion. The detailed anti-wetting performances of the literature from ref. 1 to ref. 15 are shown in Table S2. The inserted schematic diagram shows the heat transfer between impacting water and the surfaces of dense structures and nanoporous structures. Snapshots of (f) optical photos and (g) infrared photos demonstrating a high-speed water jet (21 m/s) impacting a PF10 surface at −5°C.

The conventional criterion for droplet rebound is to compare the anti-wetting capillary pressure against the dynamic impact pressure.[49, 50] At ultralow temperatures, this criterion becomes inadequate due to the influence of viscous and thermal effects. Therefore, we

View Article Online
DOI: 10.1039/D6MH00559D

analyze the process through an energy conversion perspective. In fact, the energy balance governing rebound involving adhesion work (ΔE_{w}) and energy dissipation (ΔE_{vis}) can be expressed by (Supplementary Note S3):

$$E_{\mathrm{k}}^{'} = E_{\mathrm{k}} - (\Delta E_{\text{vis-vol}} + \Delta E_{\text{vis-int}} + \Delta E_{\mathrm{w}})$$

where $E_{\mathrm{k}}^{'}$ and E_{k} are the kinetic energies of the impacting droplet and recoil droplet, respectively. $\Delta E_{\text{vis-vol}}$ and $\Delta E_{\text{vis-int}}$ are volume part and surface part of energy dissipation caused by viscous friction, respectively (Fig. S14), both of them are proportional to water viscosity.[51] The adhesion work ΔE_{w} is contingent upon intrinsic contact angle and contact angle hysteresis (Supplementary Note S4). To meet $E_{\mathrm{k}}^{'} > 0$ for droplet bouncing, the energy dissipation and adhesion work should be minimized as much as possible. The exceptional performance of our PF coatings stems from their unique structure, which addresses both terms. First, the fine nanoporous structures exhibit ultralow thermal conductivity of 58.1±0.4 W/K, with an approximately 24.6% reduction compared with pristine PF substrate (Fig. S15). This severely limits heat transfer from the droplet according to the Fourier heat conduction equation,[52] thereby preventing a drastic rise in droplet viscosity and suppressing energy dissipation.[53] Second, the nanostructures contributed to reducing contact angle hysteresis, hence decreasing the kinetic energy loss.[54] Consequently, the impacting droplet can rebound from the surface even at an extremely low surface temperature.

Owing to the reduced cost, enhanced mechanical robustness, and greater potential for practical application, PF10 was selected as the primary sample for the following tests. As shown in Fig. 3e (Movie S7), PF10 was able to repel 1.4 m/s impact droplets even when

View Article Online
DOI: 10.1039/D6MH00559D

cooled to −122°C. To further assess the resilience against more severe dynamic conditions, the PF10 was cooled to −5°C using a cold platform and subjected to a water jet at 21 m/s. The interaction was captured simultaneously by high-speed and infrared cameras at 200 and 30 frames per second, respectively. After ~900 ms of continuous jet impingement, only minimal water adhesion was observed on the PF10 surface, with the largest residual droplet being merely ~0.5 mm in diameter (Fig. 3f). Although the infrared and high-speed images were not perfectly synchronized due to the lower frame rate of the thermal camera, the infrared sequences still clearly recorded the surface temperature evolution before and after impact, as evidenced in Fig. 3g. These results indicate that PF10 maintains effective dynamic anti-wetting performance across an exceptionally broad spectrum of conditions from ultra-low temperature droplet impact to high-speed water jet impingement, highlighting its potential for real-world anti-icing applications.

2.4. Dynamic Deicing Induced by Gravity

Gravity-driven ice removal exploits a fully passive physical process, offering a low-cost and sustainable deicing strategy that requires no chemicals or external energy input. However, the ice adhesion strength between ice and superhydrophobic surfaces typically exceeds 10 kPa,[55] a value that cannot be overcome by gravitational force alone. In contrast, water droplets on superhydrophobic surfaces exhibit extremely low adhesion, enabling them to slide off at tilt angles below 5° or even 1°.[56] Therefore, transforming the solid-solid interface into a solid-liquid interface through the heating effect may enable gravity-induced dynamic deicing. We first conducted freezing-melting tests on different sample surfaces (Fig. S16). Water droplets were frozen at −15°C and subsequently allowed to melt during natural warming. The measured icing time can be determined as PF20>PF10>NS40>NS20

View Article Online
DOI: 10.1039/D6MH00559D

(Fig. 4a), which correlates directly with their dynamic anti-wetting performance observed in waterjet-impacting tests (Fig. 2h). Thus, the nanoporous structures of PF10 and PF20 confer superior performance in both static ice delay and dynamic anti-icing compared to NS20 and NS40. Subsequently, we measured the sliding angles (SAs) of the melted droplets by directly tilting the cold platform. The SAs followed the order PF20<PF10<NS40<NS20, inversely correlated with the freezing delay performances. Notably, only PF10 and PF20 surfaces retained their superhydrophobicity after the complete freezing-melting cycle, with SAs below 10°.

This divergence in deicing outcome is governed by the degree of superhydrophobicity recovery after melting. The nanoporous structures of PF10 surface coatings favor recovery of the C-B state for two synergistic reasons. First, its fine structure inherently resists water penetration and mitigates irreversible wetting transitions during freezing (Fig. 2g).[17] Second, the extended freezing time and high interfacial thermal resistance promote a pronounced temperature gradient within the melting ice droplet. This gradient drives a Marangoni flow, which facilitates the transport of air bubbles to the solid-liquid interface, actively replenishing the air layer and restoring superhydrophobicity.[57]

View Article Online
DOI: 10.1039/D6MH00559D

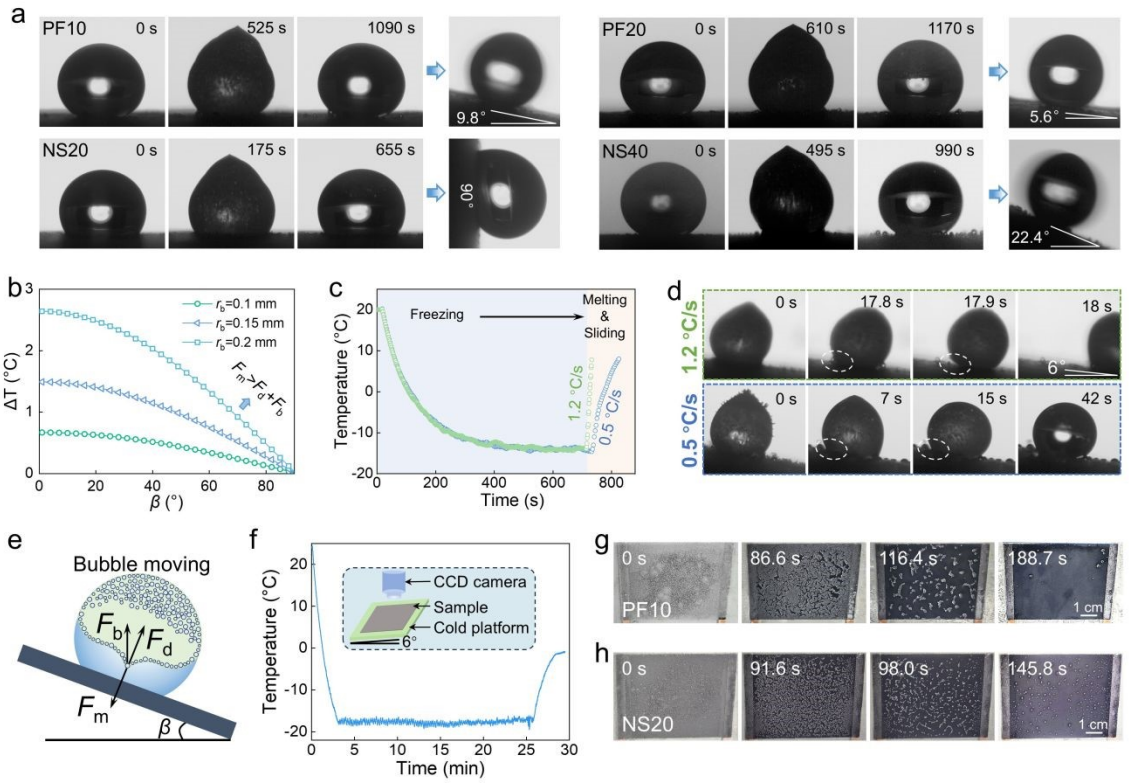

Fig. 4 (a) Images of droplets on PF10, NS20, PF20, and NS40 surfaces during the freezing/melting cycle. The right panel shows the sliding angles of the melted droplets. (b) Variation of critical temperature difference between the surface and the top unmelted ice with surface inclination angle for different bubble sizes. (c) Temperature curve of the PF10 surface with different warming rates after freezing on a cold platform. (d) Corresponding optical images showing the dynamic behaviors during the melting process of ice droplets on the PF10 surface at different warming rates. (e) Schematic diagram of force analysis of bubbles inside a melted ice droplet on inclined surfaces under the Marangoni effect. (f) Temperature curve of the sample surface during the freezing/melting cycle for frost removal tests. The inserted schematic diagram represents the test device. Snapshots of coalescence-induced wriggling of melting frosts on (g) PF10 and (h) NS20 surfaces with an inclination angle of 6°.

In the real world, ice removal is driven by the thermal-mechanical coupling effect rather than their independent action discussed above. When ice melts on an inclined surface, the condition for ice drop sliding can be expressed as:[42]

View Article Online
DOI: 10.1039/D6MH00559D

$$mg\sin\beta > \begin{cases} F_{\text{ice-solid}}, & \text{initial melting} \\ Kd\left(\cos\theta_{\text{trial}} - \cos\theta_{\text{lead}}\right) + F_{\text{ice-solid}}, & \text{intervening state} \\ Kd\left(\cos\theta_{\text{trial}} - \cos\theta_{\text{lead}}\right), & \text{interface ice melting} \end{cases}$$

where β is the surface inclination angle, m is the mass of the droplet, g is the gravitational constant, K is a dimensionless factor associated with droplet shape, d is the width of the three-phase contact line, θ_{trial} is the trial contact angle, and θ_{lead} is the lead contact angle. $F_{\text{ice-solid}}$ is the solid-solid resistance caused by adhesion between ice and the sample surface, while $Kd\left(\cos\theta_{\text{trial}} - \cos\theta_{\text{lead}}\right)$ represents the liquid-solid resistance from static contact line pinning. There are two critical sliding conditions for melting ice. In the initial melting regime, the ice-substrate interface is only partially molten, and the contact line is largely immobilized. Thus the $Kd\left(\cos\theta_{\text{trial}} - \cos\theta_{\text{lead}}\right)$ can be ignored. Sliding occurs if the gravitational shear stress overcomes the residual ice adhesion, i.e., $mg\sin\beta > F_{\text{ice-solid}}$. In the interface ice melting regime, the ice-substrate interface is fully liquefied and $F_{\text{ice-solid}}$ vanishes. The sliding of the melted droplet is determined by the depinning of the contact lines, i.e., $mg\sin\beta > Kd\left(\cos\theta_{\text{trial}} - \cos\theta_{\text{lead}}\right)$, which typically depends on a well-recovered superhydrophobicity. Real-world dynamic deicing represents an intervening state between these two conditions above. Clearly, the restoration of superhydrophobicity will simultaneously reduce the deicing resistance of both solid-solid and solid-liquid interfaces.

The underlying mechanism of superhydrophobic recovery under thermal-mechanical coupling effects can be attributed to Marangoni effects at the inclined surface. The force exerted on the bubble along the direction perpendicular to the surface is given by:[57]

$$F = F_{\text{m}} - F_{\text{b}} - F_{\text{d}} = \int_0^{2\pi} \frac{d\gamma}{dT}\Delta T \cdot r_b d\alpha - \frac{4\pi}{3}\rho g r_b^3 \cos\beta - \frac{\pi}{2}C \cdot \rho v_b^2 r_b^2$$

View Article Online
DOI: 10.1039/D6MH00559D

where F_m, F_b, and F_d are the Marangoni force, buoyancy, and water drag, respectively; $\frac{d\gamma}{dT}$, ρ, g, and C are the change rate of water's surface tension with temperature, water density, gravitational constant, and resistance coefficient of water, respectively. The temperature difference between surface and the top unmelted ice (ΔT), bubble radius (r_b), surface inclination angle (β), and moving velocity of bubble (v_b) are the four key variables affecting bubble movement towards the interface or vice versa. In the critical condition for downward motion of a bubble, the relationship between the required temperature gradient and the inclination angle of the surface is shown in the Fig. 4b. Clearly, the temperature gradient directly governs bubble migration efficiency. An inclined surface reduces the required temperature gradient to drive bubbles toward the interface, especially for larger bubbles (Figs. 4b and S17). Then the PF10 was cooled from room temperature until the sessile droplet froze, then the surface was tilted to 6° and warmed at different rates (Fig. 4c). Surprisingly, when the PF10 surface was warmed at a high heating rate (~1.2°C/s), the ice droplet slid off the surface with a remained peach-like shape (Fig. 4d). However, at a lower warming rate of ~0.5°C/s, the meltwater wetted and pinned on the surface. In fact, the faster heating establishes a steeper temperature gradient, which intensifies the Marangoni flow, allowing more and larger bubbles to impact the interface, facilitating the replenishment of the air layer (Fig. 4e).

We further extended this concept to frost removal. As shown in Fig. 4f, the same freezing/melting cycle was performed to investigate gravity-induced dynamic defrosting. During natural warming of a frosted PF10 surface tilted at 6°, the melting frost layer underwent pronounced coalescence-induced wriggling, culminating in spontaneous, large-scale detachment (Fig. 4g, Movie S8). In this case, the dynamic behaviors of melting ice

View Article Online
DOI: 10.1039/D6MH00559D

may overcome $F_{\text{ice-solid}}$ before complete interface melting, which has been confirmed by our previous work.[42] Conversely, under identical conditions, the NS20 surface exhibited higher adhesion with water/ice with more subdued coalescence-induced wriggling of chain-like water, leaving numerous water droplets on the surface (Fig. 4h, Movie S9). This comparative study conclusively demonstrates that the fine nanoporous structure of PF10 ensures not only outstanding anti-icing performance but also superior recovery of a low-adhesion state during melting, enabling efficient gravity-driven deicing and defrosting.

2.5. Icing Wind Tunnel Assessment

The icing wind tunnel is designed to produce high-speed supercooled microdroplets, thereby replicating in-flight icing conditions at high altitudes. As shown in Fig. 5a, the reflux icing wind tunnel is composed of a cooling system, water atomization system, compressor system, aerodynamic system, and test section. Test samples were fabricated as thin-walled composite airfoils that were connected to the fixture of the test section. We designed three configurations and only the leading edge was heated (Fig. S18). For PF10-PF10, both the leading edge and the downstream runback zone were coated with PF10. To compare the capabilities of different samples for suppressing overflow ice, PF10-NS20 was prepared by replacing the non-heating zone of PF10-PF10 with NS20. Additionally, PFac-NSac was fabricated as a control group that was coated with aviation paint but not superhydrophobic slurry. Infrared imaging confirmed that all heated leading edges exhibited uniform temperature distribution under a power density of 0.1 W/cm^2, establishing a consistent thermal baseline for comparative testing (Fig. 5b).

View Article Online
DOI: 10.1039/D6MH00559D

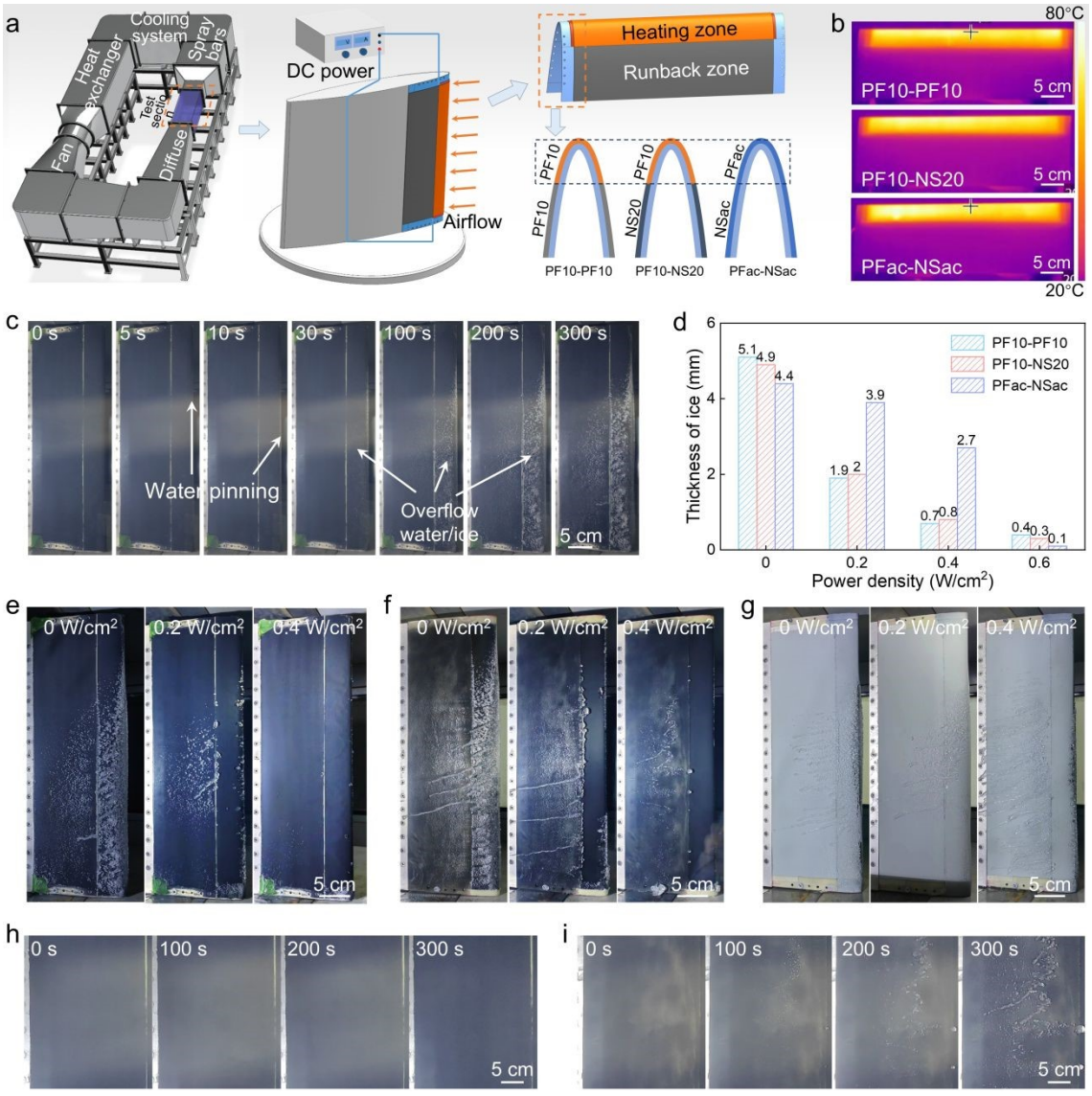

Fig. 5 (a) Schematic diagrams of icing wind tunnel test of three composite airfoil configurations: PF10-PF10, PF10-NS20, and PFac-NSac. (b) Infrared images confirming uniform temperature distribution on the heated leading edges at 0.1 W/cm^2. (c) Optical images of the icing process of PF10-PF10. (d) Variation of ice accretion thickness on the leading edge with supplied power densities. Optical images of (e) PF10-PF10, (f) PF10-NS20, and (g) PFac-NSac after icing wind tunnel tests under different electric power supplies. Optical photos of runback zones of (h) PF10-PF10 and (i) PF10-NS20 during icing wind tunnel tests.

To assess the anti-icing performance in simulated aviation conditions, these three samples were positioned in the icing wind tunnel, which was cooled to the predetermined

View Article Online
DOI: 10.1039/D6MH00559D

temperature before turning on the spraying system. During the initial spray period of 5-10 s, only sporadic adherent droplets/ice patches were observed on the leading edges of PF10-PF10, without the formation of a continuous water film or rivulet flow (Fig. 5c). However, under prolonged exposure (30-100 s) to the high flux of supercooled droplets, significant ice accretion occurred on the PF10-PF10 leading edge despite its excellent superhydrophobicity. This demonstrates that under the extreme water collection rates typical of leading edges, passive superhydrophobicity alone is insufficient to prevent ice accretion, a well-documented challenge in the field.[7] Furthermore, after a 300 s icing test at different power supplies, ice accretion thickness on different airfoil leading edges was measured. In the absence of an electrical power supply, the ice thickness reached 5.1 mm and 4.9 mm on the leading edges of PF10-PF10 and PF10-NS20, respectively (Fig. 5d), which were comparable to that of PFac-NSac (4.4 mm). However, upon applying a low power density of only 0.2 W/cm^2, ice accretion on the leading edges of both PF10-PF10 and PF10-NS20 was effectively inhibited (Fig. 5e-f), resulting in a sharp reduction in ice thickness of approximately 60% compared to their unpowered state. At a higher power density of 0.4 W/cm^2, only discontinuous, small ice particles adhered to the PF10 surfaces of the leading edges (Fig. 5e-f). These particles could be readily removed by airflow following further accumulation and growth (Movie S10). When the aviation coating was applied to the leading edge of the control group (PFac-NSac), a power density of 0.4 W/cm^2 achieved only a ~39% reduction in ice thickness. The suppression of ice accretion on this control surface required a higher power density of 0.6 W/cm^2. Therefore, the PF10-based leading edge enables a reduction in energy consumption of at least 33% relative to the conventional aviation coating. It is worth noting that the nanoporous structure exhibits a

View Article Online
DOI: 10.1039/D6MH00559D

higher thermal resistance than the sprayed aviation paint, yet it still delivers higher deicing efficiency and lower energy consumption. This result demonstrates that the contribution of the stable air layer to reducing ice adhesion outweighs the thermal resistance penalty it introduces. This observation is consistent with our previous report on the dual role of the interfacial air layer and its dominant contribution to lowering ice adhesion.[58]

Importantly, the runback zone of the airfoil usually faces milder icing conditions than the leading edge, thereby often being expected to achieve passive anti-icing without a power supply.[59] As shown in Fig. 5e-f, the runback zone of PF10-PF10 exhibited less ice accretion than that of PF10-NS20 at each supplied power density. While the aviation coating on PFac-NSac failed to suppress overflow ice formation across the tested power range (Fig. 5g). In fact, the water collection coefficient at the runback zone is relatively low, thus the surface ice accretion is mostly caused by water flow from the leading edge. Due to the excellent dynamic anti-wetting capabilities of PF10, the overflow water can be removed easily due to the highly slippery C-B state (Fig. 5h-i, Movies S10-11). Therefore, our nanoporous superhydrophobic films demonstrate a dual-mode application strategy: (1) as a low-energy enhancer for electro-thermal systems at critical areas like leading edges to drastically reduce power consumption, and (2) as a stand-alone passive solution for areas prone to runback icing.

We also collected state-of-the-art literature involving the investigation of the anti-icing/deicing performance of superhydrophobic surfaces under icing wind tunnel conditions. As shown in Table S3, without active electric heating, passive anti-icing cannot be achieved solely by the superhydrophobic effect. When combined with electric heating, the superhydrophobic effect shows a significant reduction in the required power supply.[60]

View Article Online
DOI: 10.1039/D6MH00559D

Notably, the anti-icing power density of the prepared PF10 in this work is only 0.4 W/cm^2, which is the lowest value among these reports. Although the energy saving percentage is only 33%, which appears modest compared to the enhancements reported in existing literature. This can be attributed to the specific properties of the control group, a commercial mature aviation paint that features a low surface energy and reduced intrinsic ice adhesion. These results above conclusively demonstrate the practical anti-icing capability of PF10 under simulated realistic icing conditions and highlight its promising application potential for resin-based composite materials.

3. Conclusions

In summary, this work theoretically and experimentally demonstrated the subversive advantage of nanoporous structures in inhibiting the formation and accumulation of water and ice. We elucidated the often-overlooked influence of the substrate on spray morphologies. A novel spraying strategy to construct fine nanoporous structures utilizing a porous fibrous substrate was proposed. The extreme anti-wetting properties of the resulting nanoporous films were emphasized, including their ability to repel impacting water on surfaces at ultralow temperatures (−141°C) and withstand prolonged vapor condensation (3 h). The shedding of melting and melted ice from the PF10 surfaces at tilt angles below 10° confirmed the dynamic dewetting after icing/melting cycles. Additionally, the PF10 surface exhibited excellent anti-icing performances in the icing wind tunnel, effectively suppressing leading-edge and overflow icing under an electric power density of 0.4 W/cm^2. Our earlier work centered on the superhydrophobic/electrothermal modification of fiber reinforced polymer-based composites with these PF films as substrate, and confirmed their superhydrophobic durability and mechanical properties of the

View Article Online
DOI: 10.1039/D6MH00559D

composites.[37] This facile fabrication presents a promising pathway toward practical anti-icing and deicing applications used in wind turbine blades, aircraft, and liquid hydrogen and liquid oxygen storage tanks.

4. Experimental Section

Materials: The bisphenol-A epoxy resin (E51) was purchased from Yueyang Baling Petrochemical Company. Multiwalled carbon nanotubes (MWCNTs, TNM3) were purchased from Chengdu Organic Chemicals Co., Ltd. (China). Fumed silica (SiO_2, 4-40 nm in diameter) was supplied by GRACE Davison (America). The glass fiber prepregs (1502T/EW220B) were supplied by Weihai Mingyue New Materials Co., Ltd. Organic solvents such as ethyl acetate, glycerol, ethylene glycol, methylene blue, dimethyl sulfoxide, cyclohexanone, and toluene were all bought from Macklin Biochemical Technology Co., Ltd (China). T31 curing agent was bought from Tianjin Ningping Chemical Products Co., Ltd. The porous fibrous films (CNTF1414-1, PF film) were purchased from Kunming Natai Technology Co., Ltd. The aviation paint (TS 96-75) was supplied by Tianjin Lighthouse Paint Co., LTD. All raw materials above were used without further treatment, and deionized water (18 MΩ) was used throughout the experiments.

Preparation of Nanoporous Superhydrophobic Films: Firstly, the E51 epoxy resin was fluorinated following the methodology outlined in our previous work.[61] The fluorinated E51 epoxy resin (FE51) was subsequently mixed with ethyl acetate, T31 curing agent, and nanoparticles consisting of equal proportions of SiO_2 and MWCNTs. After magnetic stirring for 10 min and ultrasonication for 20 min (VOSHIN-250W), the slurry was transferred into a spray gun. Then, taking the PF film as substrate, the spraying was implemented from a distance of ~10 cm at a pressure of ~0.3 MPa. The resin-based

View Article Online
DOI: 10.1039/D6MH00559D

composite materials were used as a nonporous substrate (NS) for the same spraying process that was fabricated by bag pressing four layers of glass fiber prepregs. For subsequent tests, the sprayed PF was integrated on the surface of the composite material by laying it on the prepregs and molding as described in previous work.[37, 62] The spraying coatings on PF and NS are designated as PFx and NSx, respectively, where x represents the content of mixed nanoparticles (measured in percentages). In addition, the sprayed commercial aviation coatings (ac) on PF and NS substrates are designated as PFac and NSac, respectively. To prepare the composite airfoils for icing wind tunnel tests, 16 layers of prepreg were laid on the surface of the mold, followed by laying the PF10 film on the specific zones before air bagging. The samples for the subsequent icing wind tunnel tests have a projected size of 150 mm in chord length and 470 mm in wingspan length. The heating zone in the leading edge (with ~30% of the surface area) has a projected size of 45 mm in the chord length and 430 mm in the spanwise length (Fig. S18).

Characterizations: The microlevel morphologies were characterized by scanning electron microscopy (SEM, Tescan Maia 3, Czech Republic) along with EDS. The thermal conductivity was measured by the thermal constant analyzer (TPS2500S, Sweden) using hotdisk method according to ISO 22007-2. Contact angle (CA, represented by θ) and sliding angle (SA, represented by θ_s) were measured by the optical measuring meter (SL200KS Solon, China). At least 3 randomly different locations were tested to demonstrate the repeatability of the measurements. For the tests of CA and SA at low temperatures, the sample was placed on the cold platform and cooled to the set temperature, followed by performing the same measurement procedure. The surface temperature was monitored by the PT100 thermometers, whose probe was a patch-type and could be

View Article Online
DOI: 10.1039/D6MH00559D

adhered to the sample surface. Alternatively, the infrared images/videos were captured with an infrared camera (FOTRIC 626CH) to obtain the macroscopic temperature distribution.

Water Impact Test: To investigate the dynamic anti-wetting performances, a water droplet was released from ~10 cm to impact the sample surfaces (Fig. S19). The impacting process was recorded by a high-speed camera (SH3 Mini, Shenzhen SINCEVISION Technology Co., Ltd.). The humidity of the test environments was 55±3%, and the room temperature was 20°C. The surface temperature of the sample was controlled by the cold platform (TEC1-12706) and tested by the PT100 or infrared camera. For the anti-wetting test in the ultralow-temperature icing environments, liquid nitrogen was used to cool the samples on the copper cylinder, which was tilted to ~5° to facilitate the observation of the dynamic behavior of droplets. The temperature of the sample surface was monitored by the PT100 thermometer. To investigate the long-term anti-wetting performance in condensation environments, the test setup was sealed, and a humidifier was employed to maintain a relative humidity at 60±5%. Then the sample surface was controlled at −5±1°C, and the evolution of surface condensation was observed by optical microscope (HG-3101U, Wuxi Hanguang Optics Co., Ltd).

Icing and Deicing Test: The freezing time of droplets (~20 μL) on the low-temperature surfaces was tested by the contact angle meter (Fig. S20). Firstly, the samples were cooled to the predetermined temperatures on a cold platform before placing the droplet at room temperature. The testing environment was maintained at a relative humidity of ~20% and an ambient temperature of ~20°C. After the droplets froze, the cold platform was turned off to observe the melting behaviors of ice droplets. Then the sliding angle was tested by tilting the cold platform after the sample surface returned to room temperature.

View Article Online
DOI: 10.1039/D6MH00559D

Additionally, to investigate the effect of the high-humidity environment (55±3%) on the freezing/melting process, droplets were placed on the sample surfaces at room temperature before turning on the cold platform. After the droplets were frozen, turn off and tilt the cold platform by 6° to observe the dynamic behavior of the melting ice droplets. The warming rate of the sample surface was controlled by the electric heating substrate. The surface test temperature was monitored by a patch-type temperature sensor (PT100). In addition, the dynamic behavior of melting ice droplets was directly observed through an optical microscope.

Icing Wind Tunnel Test: The icing wind tunnel was used to assess the dynamic icephobic properties in a simulated flight icing environment. Every test follows the same experimental parameters, i.e., air temperature of −6±0.5°C, wind speed of 20 m/s, liquid water content (LWC) of 2.82 g/m^3, and median volume diameter (MVD) of 20 μm. After turning on the electric heating for ~5 min to reach a relatively stable working state, the water spray system was turned on for 300 s to evaluate the effectiveness of various anti-icing/deicing strategies. To optimize the supply of electric heating power, the heated leading edge constitutes 30% of the total airfoil surface area. The icing behaviors of the test surface were captured by a digital camera. A power supply (LW-K3010D) was used to perform controlled electric heating. The reported power densities represent the power supplied to the heating element and are calculated from the output voltage and current displayed by the power supply.

Author contributions

Yunyun Meng: Conceptualization, Data curation, Formal analysis, Investigation, Methodology, Validation, Visualization, Writing - Original draft, Writing - Review &

View Article Online
DOI: 10.1039/D6MH00559D

Editing. **Zhengang Pu:** Data curation, Validation, Visualization, Writing - Review & Editing. **Yang Qi:** Data curation, Validation, Visualization, Writing - Review & Editing. **Yanxin Zhang:** Data curation, Investigation, Methodology, Validation, Writing - Review & Editing. **Suli Xing:** Conceptualization, Methodology, Project administration, Resources, Supervision, Writing - Review & Editing. **Xian Yi:** Conceptualization, Project administration, Resources, Writing - Review & Editing. **Song Wang:** Conceptualization, Methodology, Project administration, Supervision, Writing - Review & Editing. **Senyun Liu:** Methodology, Resources, Supervision, Writing - Review & Editing. **Nan Wu:** Conceptualization, Formal analysis, Funding acquisition, Methodology, Project administration, Supervision, Writing - Review & Editing.

Data Availability

All data generated or analyzed during this study are included in this published article and its supplementary information (SI).

Declaration of Competing Interest

The authors declare that they have no known competing financial interests or personal relationships that could have appeared to influence the work reported in this paper.

Acknowledgements

This work was supported by Hunan ProvincialNatural Science Foundation of China (2021JJ30028, 2026JJ50040), National Natural Science Foundation of China (U2570220), and the Science and Technology Innovation Program of Hunan Province (2023RC3006).

References

1. A. Dhyani, W. Choi, K. Golovin and A. Tuteja, Matter, 2022, 5, 1423-1454.

View Article Online
DOI: 10.1039/D6MH00559D

2. X. Huang, N. Tepylo, V. Pommier-Budinger, M. Budinger, E. Bonaccurso, P. Villedieu and L. Bennani, Prog. Aerosp. Sci., 2019, 105, 74-97.
3. Y. Liu, Y. Wu, S. Liu and F. Zhou, ACS Mater. Lett., 2021, 4, 246-262.
4. Z. Yu, H. Zhang, Y. Yang, B. Wang and Z. Guo, Mater. Today, 2025, 88, 906-932.
5. F. Chu, Z. Hu, Y. Feng, N. C. Lai, X. Wu and R. Wang, Adv. Mater., 2024, 36, 2402897.
6. C. Zhang, K. Pei, T. Sheng, M. Zhang, Z. Zhao, W. Huang, Y. Li, S. Ai and Z. Guo, Adv. Funct. Mater., 2025, 36, e12239.
7. Z. Tian, L. Wang, D. Zhu, C. Chen, H. Zhao, R. Peng, H. Zhang, P. Fan and M. Zhong, ACS Appl. Mater. Interfaces, 2023, 15, 6013-6024.
8. M. J. Kreder, J. Alvarenga, P. Kim and J. Aizenberg, Nat. Rev. Mater., 2016, 1, 15003.
9. D. Li, L. Wang, R. Peng, Z. Song, Z. Liu, Z. Chang, H. Zhang, P. Fan and M. Zhong, Adv. Sci., 2025, 12, e08272.
10. Y. Meng, J. Yang, X. Cui, Z. Pu, L. Wei, Y. Qi, P. Zhang, S. Xing, X. Deng and N. Wu, Adv. Colloid Interface Sci., 2026, 354, 103900.
11. P. Lyu, W. Shi, Y. Liu, R. Ding, J. Hu, B. Shang, H. Pan, J. Ren, X. Liu and W. Xu, Adv. Funct. Mater., 2025, 35, 2421174.
12. P. Sarkiris, V. Constantoudis, K. Ellinas, C. W. E. Lam, A. Milionis, J. Anagnostopoulos, D. Poulikakos and E. Gogolides, Adv. Funct. Mater., 2023, 34, 2306756.
13. H. Bai, X. Wang, Z. Li, H. Wen, Y. Yang, M. Li and M. Cao, Adv. Mater., 2023,

View Article Online
DOI: 10.1039/D6MH00559D

35, e2211596.

14. S. Xuan, H. Yin, G. Li, Z. Zhang, Y. Jiao, Z. Liao, J. Li, S. Liu, Y. Wang, C. Tang, W. Wu, G. Li and K. Yin, ACS Nano, 2023, 17, 21749-21760.
15. S. Jiang, Y. Diao and H. Yang, Adv. Colloid Interface Sci., 2022, 308, 102756.
16. R. Gao, M. Song, C. Y. H. Chao, S. Lin, L. Zhang and X. Zhang, Appl. Therm. Eng., 2024, 236, 121691.
17. R. Wen, Q. Li, J. Wu, G. Wu, W. Wang, Y. Chen, X. Ma, D. Zhao and R. Yang, Nano Energy, 2017, 33, 177-183.
18. L. Wang, D. Li, G. Jiang, X. Hu, R. Peng, Z. Song, H. Zhang, P. Fan and M. Zhong, ACS Nano, 2024, 18, 12489-12502.
19. J. Wu, C. Li, J. Dai and Y. Yan, Nat. Commun., 2025, 16, 9793.
20. M. Ouyang, R. Guo, Y. Fan, Y. Zhou, C. Wu, L. Chen, S. Huang and X. Tian, Nano Res., 2022, 16, 589-598.
21. A. B. Tesler, S. Kolle, L. H. Prado, I. Thievessen, D. Böhringer, M. Backholm, B. Karunakaran, H. A. Nurmi, M. Latikka, L. Fischer, S. Stafslien, Z. M. Cenev, J. V. I. Timonen, M. Bruns, A. Mazare, U. Lohbauer, S. Virtanen, B. Fabry, P. Schmuki, R. H. A. Ras, J. Aizenberg and W. H. Goldmann, Nat. Mater., 2023, 22, 1548-1555.
22. T.-B. Nguyen, S. Park and H. Lim, Appl. Surf. Sci., 2018, 435, 585-591.
23. L. Chen, L. Li and X. Zhang, Nat. Commun., 2025, 16, 2228.
24. X. Li, L. Chen, Y. Ma, D. Weng, Z. Li, L. Song, X. Zhang, G. Yu and J. Wang, Adv. Funct. Mater., 2022, 32, 2205462
25. S. Wu, Y. Du, Y. Alsaid, D. Wu, M. Hua, Y. Yan, B. Yao, Y. Ma, X. Zhu and

View Article Online
DOI: 10.1039/D6MH00559D

X. He, Proc. Natl. Acad. Sci. U. S. A., 2020, 117, 11240-11246.

26. L. Li, J. Wei, J. Zhang, B. Li, Y. Yang and J. Zhang, Sci. Adv., 2023, 9, eadj1554.
27. S. He, Y. Tian, H. Zhou, M. Zhu, C. Li, B. Fang, Z. Hong and X. Jing, Adv. Funct. Mater., 2025, 35, 2420369.
28. X. Deng, L. Mammen, H. J. Butt and D. Vollmer, Science, 2012, 335, 67-70.
29. D. Ranjan, A. Zou and S. C. Maroo, Chem. Eng. J., 2023, 455, 140527.
30. C. Peng, Z. Chen and M. K. Tiwari, Nat. Mater., 2018, 17, 355-360.
31. W. Zhang, S. Li, D. Wei, Z. Zheng, Z. Han and Y. Liu, J. Mater. Sci. Technol., 2024, 186, 231-243.
32. J. Wei, J. Zhang, X. Cao, J. Huo, X. Huang and J. Zhang, Nat. Commun., 2023, 14, 2862.
33. W. Jung, Y. H. Jung, P. V. Pikhitsa, J. Feng, Y. Yang, M. Kim, H. Y. Tsai, T. Tanaka, J. Shin, K. Y. Kim, H. Choi, J. Rho and M. Choi, Nature, 2021, 592, 54-59.
34. C. Zhou, L. Shan, Q. Nan, J. Zhang, Z. Fan, B. Tang, J. Li, J. Yang, H. Zhang, Z. Kang, X. Tian and X. Shi, Adv. Funct. Mater., 2024, 34, 2312696.
35. G. Heydari, M. Sedighi Moghaddam, M. Tuominen, M. Fielden, J. Haapanen, J. M. Makela and P. M. Claesson, J. Colloid Interface Sci., 2016, 468, 21-33.
36. Y. Wang, B. Lebon, I. Tzanakis, Y. Zhao, K. Wang, J. Stella, T. Poirier, G. Darut, H. Liao and M. P. Planche, Ultrason. Sonochem., 2019, 52, 336-343.
37. Y. Meng, N. Wu, Y. Zhang, J. Yang, S. Wang, S. Xing, S. Liu and X. Yi, Compos. Sci. Technol., 2025, 264, 111121.
38. A. Azimi Yancheshme, G. Momen and R. Jafari Aminabadi, Adv. Colloid

View Article Online
DOI: 10.1039/D6MH00559D

Interface Sci., 2020, 279, 102155.

39. R. Wang, F. Wu, D. Xing, F. Yu and X. Gao, ACS Appl. Mater. Interfaces, 2020, 12, 24512-24520.
40. P. Papadopoulos, L. Mammen, X. Deng, D. Vollmer and H. J. Butt, Proc. Natl. Acad. Sci. U. S. A., 2013, 110, 3254-3258.
41. W. Xu and C. H. Choi, Phys. Rev. Lett., 2012, 109, 024504.
42. Y. Meng, S. Xing, N. Wu, P. Zhang, X. Cui, X. Liang and S. Wang, ACS Mater. Lett., 2024, 6, 1457-1466.
43. Z. Li, M. Cao, P. Li, Y. Zhao, H. Bai, Y. Wu and L. Jiang, Matter, 2019, 1, 661-673.
44. Y. Meng, S. Xing, Z. Weng, S. Wang, X. Yi and N. Wu, Chem. Eng. J., 2023, 476, 146384.
45. M. Mao, J. Wei, B. Li, L. Li, X. Huang and J. Zhang, Nat. Commun., 2024, 15, 9610.
46. C. Zhang, H. Xie, Y. Du, X. Li, W. Zhou, T. Wu and J. Qu, Adv. Funct. Mater., 2023, 33, 2213398.
47. S. Shi, C. Lv and Q. Zheng, ACS Appl. Mater. Interfaces, 2019, 11, 43698-43707.
48. X. Yan, Z. Huang, S. Sett, J. Oh, H. Cha, L. Li, L. Feng, Y. Wu, C. Zhao, D. Orejon, F. Chen and N. Miljkovic, ACS Nano, 2019, 13, 4160-4173.
49. T. Deng, K. K. Varanasi, M. Hsu, N. Bhate, C. Keimel, J. Stein and M. Blohm, Appl. Phys. Lett., 2009, 94, 133109.
50. A. Checco, A. Rahman and C. T. Black, Adv. Mater., 2014, 26, 886-891.
51. R. Nishimura, K. Hyodo, H. Mayama, S. Yokojima, S. Nakamura and K. Uchida,

View Article Online
DOI: 10.1039/D6MH00559D

Commun. Chem., 2019, 2, 90.

52. G. Han, T. B. Nguyen, S. Park, Y. Jung, J. Lee and H. Lim, ACS Nano, 2020, 14, 10198-10209.
53. L. Mishchenko, B. Hatton, V. Bahadur, J. A. Taylor, T. Krupenkin and J. Aizenberg, ACS Nano, 2010, 4, 7699-7707.
54. Y. Shen, J. Tao, H. Tao, S. Chen, L. Pan and T. Wang, ACS Appl. Mater. Interfaces, 2015, 7, 20972-20978.
55. C. Chen, Z. Tian, X. Luo, G. Jiang, X. Hu, L. Wang, R. Peng, H. Zhang and M. Zhong, ACS Appl. Mater. Interfaces, 2022, 14, 23973-23982.
56. F. Yu, D. Wang, J. Yang, W. Zhang and X. Deng, Accounts of Materials Research, 2021, 2, 920-932.
57. L. Wang, Z. Tian, G. Jiang, X. Luo, C. Chen, X. Hu, H. Zhang and M. Zhong, Nat. Commun., 2022, 13, 378.
58. Y. Meng, Z. Pu, B. Ji, S. Xing and N. Wu, Int. J. Heat Mass Transfer, 2026, 264, 128731.
59. H. Sun, G. Lin, H. Jin, X. Bu, C. Cai, Q. Jia, K. Ma and D. Wen, Renewable Energy, 2021, 179, 1179-1190.
60. Y. Qi, Y. Meng, Z. Pu, L. Wei, S. Xing and N. Wu, Mater. Today Commun., 2025, 49, 113780.
61. B. Wu, J. Lyu, C. Peng, D. Jiang, J. Yang, J. Yang, S. Xing and L. Sheng, Chem. Eng. J., 2020, 387, 124066.
62. Y. Meng, S. Xing, J. Tang, H. Liu, J. Lyu, S. Wang, C. Yin, X. Yi and N. Wu, Prog. Org. Coat., 2023, 174, 107224.

View Article Online
DOI: 10.1039/D6MH00559D

1